HEALTH AND MEDICINE

A model of guided cell self-organization for rapid and spontaneous formation of functional vessels

L. Andrique[1,2*†], G. Recher[3,4†], K. Alessandri[4], N. Pujol[1,2], M. Feyeux[4], P. Bon[3,4], L. Cognet[3,4], P. Nassoy[3,4*‡], A. Bikfalvi[1,2*‡]

Most achievements to engineer blood vessels are based on multiple-step manipulations such as manual sheet rolling or sequential cell seeding followed by scaffold degradation. Here, we propose a one-step strategy using a microfluidic coextrusion device to produce mature functional blood vessels. A hollow alginate hydrogel tube is internally coated with extracellular matrix to direct the self-assembly of a mixture of endothelial cells (ECs) and smooth muscle cells (SMCs). The resulting vascular structure has the correct configuration of lumen, an inner lining of ECs, and outer sheath of SMCs. These "vesseloids" reach homeostasis within a day and exhibit the following properties expected for functional vessels (i) quiescence, (ii) perfusability, and (iii) contractility in response to vasoconstrictor agents. Together, these findings provide an original and simple strategy to generate functional artificial vessels and pave the way for further developments in vascular graft and tissue engineering and for deciphering the angiogenesis process.

INTRODUCTION

Three-dimensional (3D) cell cultures are emerging as a necessary approach to faithfully capture the behavior of cells in vivo and to improve our understanding of the fundamental cellular mechanisms under conditions that recapitulate the 3D architecture of an organ (*1*). These efforts are in line with those stemming from tissue engineering aiming at manufacturing artificial tissues and organs for regenerative medicine (*2*) and animal-free drug testing (*3*). The advancement of microfluidics and 3D printing technology applied to biological material has largely contributed to the recent development of organs-on-chips (*4*, *5*) and bioprinted tissues and organs (*6*). The goal of organs-on-chips is not per se to recreate an organ but to model some basic physiological or pathological functions by designing a minimal system that includes fine control of the environment (perfusion, stretching, and drug circulation) (*4*). By contrast, bioprinting allows recapitulation of the organ or tissue shape, internal architecture, and function by combining a proper design of the 3D-printed templates (in terms of biocompatibility, degradability, and mechanical properties) with a sequential positioning strategy of cellular and environmental components (*7*). Among the variety of recent achievements, two remarkable "tours de force" may be highlighted, namely, the reconstruction and implantation of a human external ear (*8*) and the fabrication of centimeter-thick vascularized tissues (*9*). These seemingly complex structures are built with no more than three cell types and two types of matrices. The underlying assumption in bioprinting is that positioned cells do not particularly reorganize throughout a developmental process (*10*). For this reason, it is crucial to reduce this likelihood by limiting the number of integrated cell types. As a corollary, the physiological relevance may also be altered. For instance, in an attempt to produce thick tissues that need to be vascularized to avoid necrosis due to restricted nutrients diffusion, the vast majority of current approaches consist in using only endothelial cells (ECs) and thus forming, strictly speaking, endothelial tubes (*9*). These tubular endothelial structures only partially mimic blood vessels, both in terms of cellular composition and functional properties: They ensure perfusability but fail to recapitulate the elasticity and contractility of blood vessels that are required for accommodating the pulsatile blood flow. An alternative to the all-in-one bioprinting strategy leading to minimal systems is to pursue a bottom-up approach in which multicellular modules are separately generated and subsequently assembled or printed into a more complex tissue (*11*).

A key step is to produce artificial well-organized vessels around which desired nonvascularized tissues can be grown or which can be used for vessel grafting. More specifically, in vitro blood vessels can be regarded as tubular tissues that exhibit (i) an organized histological two-layered structure comprising a layer of smooth muscle cells (SMCs) enveloping a layer of ECs around a lumen and functional properties such as (ii) contractility upon relevant stimuli and (iii) perfusability.

Previous works aiming at engineering blood vessels as two-layered tubular structures are based on elegant multiple-step manipulation including cell embedding in matrices, sheet rolling, or scaffold degradation (*2*, *12*). Here, we propose a one-step procedure to produce mature functional blood vessels. Our scheme relies on directed self-assembly of SMCs and ECs within a tubular immune-protective alginate scaffold coated with an extracellular matrix (ECM). ECs and SMCs have indeed been previously shown to self-organize when mixed together (*11*). However, the resulting cellular organization is a multicellular spheroid with SMCs being enveloped by ECs and with no lumen. This inverse configuration is consistent with the differential adhesion hypothesis (DAH) explaining that spheroids of highly contractile cells (such as SMCs), which exhibit a higher surface tension than spheroids of less contractile cells (such as ECs), are preferably screened from contact with culture medium to reduce the surface energy of the binary cellular mixture (*13*). To bias the outcome predicted by the DAH and guide cell self-assembly toward a correct vessel configuration, we have

[1]LAMC, Laboratoire de l'Angiogenèse et du Microenvironnement des Cancers (Inserm U1029) F-33170 Pessac, France. [2]Université de Bordeaux, F-33170 Pessac, France. [3]LP2N, Laboratoire Photonique Numérique et Nanosciences, Univ. Bordeaux, F-33400 Talence, France. [4]Institut d'Optique Graduate School & CNRS UMR 5298, F-33400 Talence, France.
*Corresponding author. Email: andreas.bikfalvi@u-bordeaux.fr (A.B.); pierre.nassoy@u-bordeaux.fr (P.N.); laetitiaandrique@hotmail.com (L.A.)
†These authors contributed equally to this work.
‡These authors contributed equally to this work.

designed a strategy that allows us to make dominant the interfacial energy of the boundary between the ECM and a tissue composed of only one type of cells in the self-organization process, as proposed by Gartner and co-workers (*14*). More concretely, using a 3D-printed microfluidic coextrusion device, we produced long permeable hydrogel tubes in which ECs and SMCs were coencapsulated in the presence of an ECM. Microvessels, which we named "vesseloids," of about 300 μm in diameter were formed and exhibit the main properties of mature blood vessels. In particular, (i) the typical histology of vessels is obtained within 1 day, (ii) the overall cell population becomes quiescent after a few days, and the vesseloids are (iii) perfusable and (iv) contractile in response to vasoconstrictor agents.

These artificial blood vessels are valuable models to study vessel formation and cell polarization in 3D at both morphological and molecular levels and to elucidate the implicated signaling pathways under standard conditions or in response to mechanical forces or drugs. Moreover, our vesseloids that are neither embedded in bulk ECM nor plated within the cast of a solid chip (glass, plastic, or silicone-based) can be readily handled, which opens numerous practical applications in vascularized tissue engineering, vascular grafts, and, ultimately, regenerative medicine.

RESULTS

SMC and EC-laden tubes internally coated with ECM are formed in a single-step procedure

The method to fabricate core-shell alginate fibers using a coextrusion microfluidic device was inspired from previous works of the Takeuchi group (*15*). It also extends to tubular fibers—our previous work on cell encapsulation—that consisted in coating the internal wall of spherical alginate microcapsules with ECM (*16*). Briefly, the process is based on the use of a 3D-printed chip that allowed generating triple-coaxial laminar flows (Fig. 1A). The viscous alginate solution (AL) is injected into the outer channel, the core cell suspension (CCS) in ECM-containing solution is flowed into the inner channel, and an intermediate D-sorbitol solution (IS) solution is dispensed into the intermediary channel to avoid internal alginate cross-linking due to cellular calcium release. The custom-designed chip (Fig. 1A, fig. S1, and data file S1) is immersed into the calcium bath to avoid surface tension effects that favor jet fragmentation into droplets due to the Rayleigh-Plateau instability. We chose human umbilical vein ECs (HUVECs) and vascular SMCs (vSMCs) as models for ECs and SMCs, respectively, and selected Matrigel as an ECM substitute. In the first series of experiments reported here, the cell fraction contained in the CCS was set to about 33% of the core suspension volume. Before encapsulation, cells were dispersed in liquid Matrigel at 4°C. The composition of the cell mixture was varied and finally set in the following proportions of 2:1 EC/SMC, which we found optimal. In particular, the formation of a homogeneous EC monolayer was impaired with lower EC proportions (e.g., EC/SMC = 1:1). These conditions allowed us (i) to generate a uniform and continuous micrometer-thick Matrigel coating of the tubular capsule internal wall (fig. S2) upon cross-linking of the alginate tube in a hot (T = 37°C) calcium bath and (ii) to rapidly achieve the complete cellular coverage of the internal tube surface. Upon coinjection and exit from the nozzle, rapid gelation of the alginate sheath ensured entrapment of the binary cell mixture (Fig. 1B, day 0). We observed random distribution of cells and granular rendering by phase contrast microscopy at day 0. These morphological features underwent a marked change characterized by the emergence of a layered structure before day 1 (Fig. 1B, day 1). By transducing HUVECs (nuclear eBFP2) and vSMCs (nuclear Tomato), we aimed at monitoring the dynamics of vesseloid formation. By starting live imaging 2 hours after encapsulation, we observed that, although lumen was already formed, both HUVECs and vSMCs remained very dynamic for 22 hours (movie S1), suggesting profound and rapid reorganizations toward a homeostatic configuration. The external diameter of the tube is set by the size of the nozzle exit. In this work, we produced meter-long tubes starting from 14 million ECs and 7 million SMCs (2:1 ratio) and using devices with nozzle diameters of 300, 350, and 450 μm. The corresponding external alginate tube diameters were 265 ± 11 μm, 360 ± 11 μm, and 448 ± 12 μm, indicating slight alginate shrinkage upon gelation (fig. S3) (*17*). The inner tube diameter, which is related to the size of the vesseloid lumen, was then derived from the alginate wall thickness (Fig. 1, C and D). Because of volume conservation in the composite jet, we theoretically expect the ratio between the AL flow rate and the IS + CCS flow rate to be the sole tuning parameter. Nonetheless, in practice, not only did the total flow rate also affect the morphology and uniformity (e.g., the absence of bulges) of the tube, but also, for a given total flow rate, we observed the shell thickness to slightly vary upon relative tuning of the three coflow rates (Fig. 1C). We performed all the experiments reported here by empirically optimizing the flow conditions. For instance, using a device with a nozzle of 450 μm in diameter, we found that flow rates of 2 ml hour^{-1} (for AS) and 1 ml hour^{-1} (for IS and CCS) were appropriate to produce uniform tubes over macroscopic lengths. Their outer tube diameter was D_{out} = 448 ± 12 μm, and the inner tube diameter was D_{in} = 321 ± 21 μm (Fig. 1E).

Rapid and spontaneous cellular organization leads to vesseloids structurally resembling mature blood vessels

To quantitatively characterize cell self-organization inside the vesseloids, we performed in toto immunostaining and fluorescence confocal microscopy. We used cell type–specific antibodies including endothelial anti-CD31 and α-smooth muscle actin (αSMA; Fig. 2A). As seen in the optical and transverse sections, a lumen was formed at day 1 (Fig. 2, A and B). Moreover, as depicted by immunostaining, cells were sorted out within 1 day into a two-layered architecture comprising an internal layer of HUVECs mostly lining the lumen and an external layer mainly composed of vSMCs facing the unlabeled alginate shell (Fig. 2A). Some internal remnants of cells debris were sometimes found, suggesting incomplete removal of cells that have not integrated the self-assembled structure. This observation was reinforced by a quantitative image analysis (Fig. 2C). We measured the fluorescence intensity profiles averaged over a strip of 10 pixels in width for both HUVEC and vSMC staining. Since vesseloid sections are not perfectly circular and because of variability from one tube to another, the profiles were first registered by taking the interface between the two peaks (Fig. 2C, n = 4 tubes) as a reference. This allowed us to derive the image of an "average tube." We found two well-separated intensity profiles, confirming the correct histological position of the two cell populations. Last, additional immunostaining of laminin, which is a native component of Matrigel, together with CD31 and αSMA shows that Matrigel is visible at day 1 and that vSMCs are intimately anchored into the ECM-like layer, as evidenced by the orange/yellow coloration of vSMCs, suggesting a strong affinity of vSMCs for laminin (Fig. 2D). Note that vSMC coverage is mono- or submonolayered. This configuration is a direct

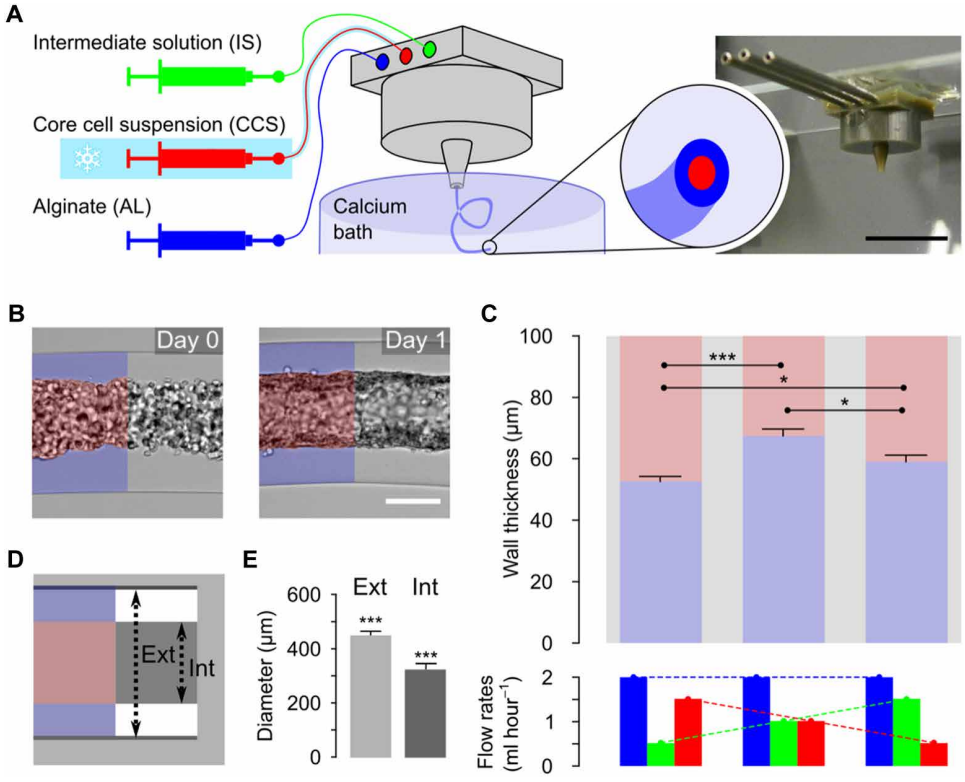

Fig. 1. 3D vascular fabrication process. (**A**) Drawing of the microfluidic platform and picture of the coextrusion device. The three solutions are injected simultaneously by a computer-controlled pump, inside a 3D-printed device soaking in a 100 mM calcium bath; 2.5% AL, IS, and CCS (HUVEC/SMC/ECM). Scale bar, 1 cm. (**B**) Cell-laden tube after production (day 0) or after 1 day of culture (day 1). Scale bar, 200 µm. (**C**) Measurements of the alginate wall thickness of alginate tubes produced with a 450-µm nozzle exit coextrusion device for the following injection flow rates ($n = 8$): 2 ml hour^{-1} (AL), 1 ml hour^{-1} (IS), and 1 ml hour^{-1} (CCS); 2 ml hour^{-1} (AL), 1.5 ml hour^{-1} (IS), and 0.5 ml hour^{-1} (CCS); or 2 ml hour^{-1} (AL), 0.5 ml hour^{-1} (IS), and 1.5 ml hour^{-1} (CCS). (**D** and **E**) Tube formation reproducibility: Measurements of external and internal diameters along the same tube, separated by at least 1 mm ($n = 16$). Photo Credit: Laetitia Andrique (INSERM U1029), Gaelle Recher (CNRS UMR 5298).

consequence of the reduced number of encapsulated vSMCs as compared to ECs and, most likely, of the use of Matrigel that favors the nonproliferative contractile phenotype of vSMCs (*18*).

Moreover, we investigated whether vesseloids have already formed an elastic lamina after culture for 1 day. Immunostaining using anti-elastin antibodies was negative, as expected for the early stages of vessel formation. However, we detected fibrillin when tissues were probed with anti–fibrillin-1 antibody (fig. S4A), suggesting the onset of production of elastic lamina components. As another important evidence that vesseloids organize into mature blood vessels within 1 day, we observed that vascular endothelial (VE)-cadherin was strongly expressed and colocalized with CD31 in HUVECs (fig. S4B), indicating the formation of adhesive contacts between neighboring cells within the EC monolayer.

Last, to pursue a thorough critical test of the significance of the vesseloid model, we aimed at determining whether a variety of other molecular features of native vessels was recapitulated here. These include the expression of (i) basal and luminal markers [e.g., integrin β1 and podocalyxin (PODXL)], (ii) arterial and venous markers neuropilin-1,2 (NRP1/NRP2), and (iii) endothelial activation markers [vascular cell adhesion molecule-1 (VCAM-1) and intercellular adhesion molecule–1 (ICAM-1)] in regular culture conditions and in response to inflammatory stimuli. We first analyzed the expression of integrin beta-1 (ITGβ1 basal marker) and PODXL (luminal marker) in 3D vesseloids compared to 2D cultures by reverse transcription quantitative polymerase chain reaction (RT-qPCR; fig. S5A). Expression of both markers was significantly enhanced by 1.5- and 2.5-fold, respectively, as compared to 2D control. Similarly, the expression of ICAM-1 and vascular cell adhesion molecule–1 (VCAM-1), two typical markers of an activated endothelium, was markedly increased in ECs from vesseloids compared to ECs cocultured 2D with SMCs, after CD31^{+} cell magnetic bead cell sorting (fig. S5B): 401-fold (ICAM-1) and 3.72-fold (VCAM-1). Upon inflammatory cytokine stimulation with interleukin-1β or tumor necrosis factor–α (fig. S5C), ICAM-1 and VCAM-1 expressions are also increased in a dose-dependent manner. Together, these control experiments strongly suggest the rapid formation of an activable endothelium in vesseloids. In addition, we investigated whether vesseloids express arterial and/or venous markers (NRP1 and/or NRP2). From RT-qPCR analysis, we found that both markers were expressed at levels similar to 2D cultures, but with a prevalence of NRP1 (two fold), suggesting that HUVECs mainly maintain an arterial-like phenotype in vesseloids (fig. S5D). On the basis of the well-known plasticity of ECs in culture even for a short time (*19*), coculture with coronary artery SMCs has very likely promoted this arterial phenotype.

Longer-term evolution reveals vascular homeostasis

As shown above, vesseloids readily acquired the histological structure of mature blood vessels. However, whether this supracellular organization was in a homeostatic state similar to the one of mature

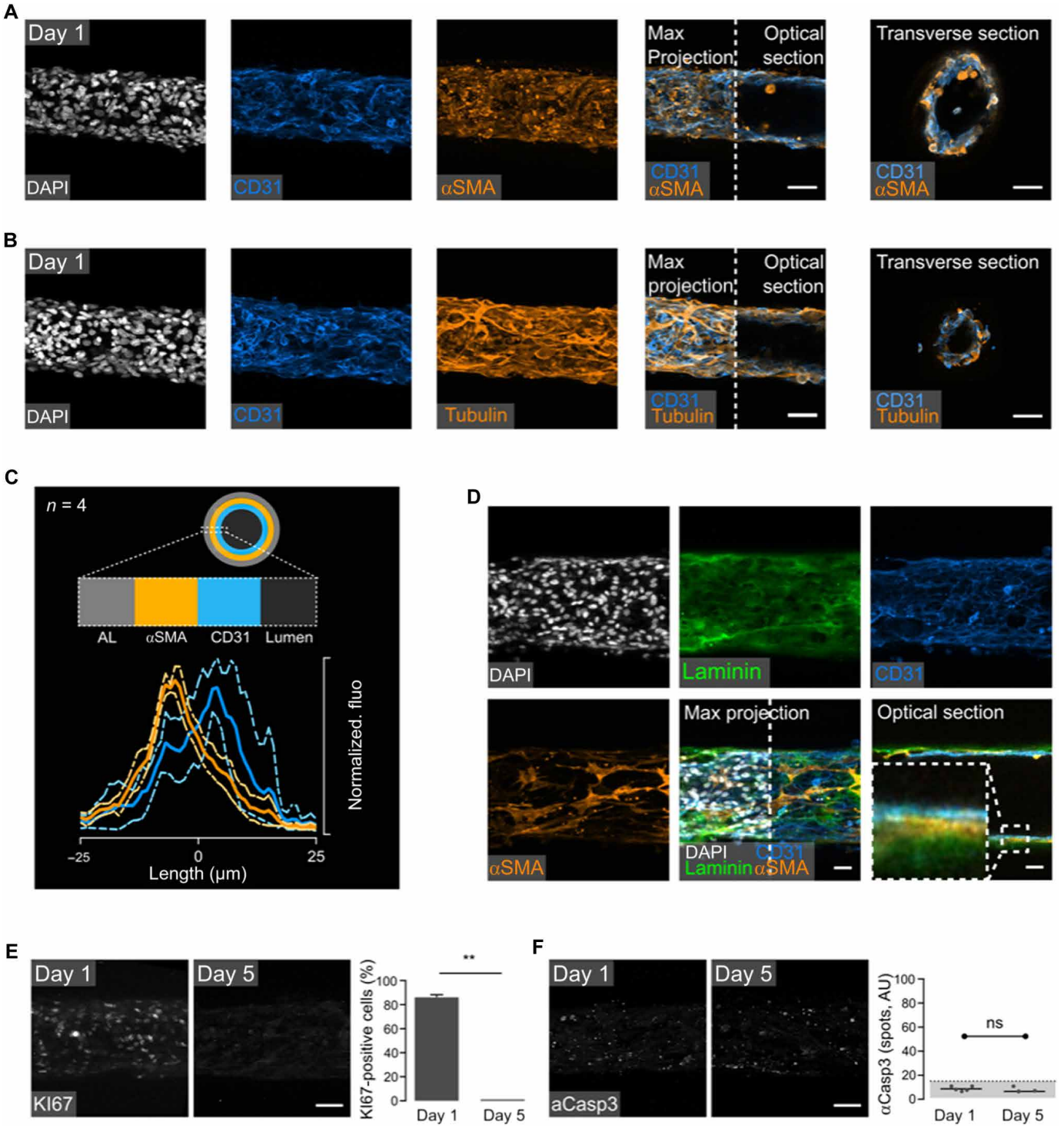

Fig. 2. Self-organization into artificial mature blood vessels. (**A** and **B**) Confocal imaging of vesseloid immunostainings at day 1. Nuclei are gray (DAPI), CD31 is blue (endothelial marker), and αSMA or tubulin labeling is orange. Images correspond to a maximal intensity projection along the *z* axis, except for the half panels indicated as "optical section," which depict a representative image at the equatorial plane. Scale bars, 50 μm. (**C**) Fluorescence intensity profiles of αSMA and CD31. The four different measurements were aligned together based on the intersection between both intensity distributions, and this value was taken as the reference in the plot. Negative values indicate distance toward the alginate wall, and positive values indicate distance in the direction of the lumen. (**D**) Anchoring of SMCs in ECM. Immunostaining of laminin, CD31, and αSMA was performed. Images correspond to a projection of the *z* axis of each signal. Nuclei are in gray (DAPI), laminin in green, CD31 endothelial marker in blue, and αSMA in orange. Zoom of an equatorial section of the vesseloid. Scale bars, 100 μm. (**E**) KI67 nuclear signal and histogram representation of proliferation at days 1 and 5. (**F**) Activated caspase-3 signal and histogram representation of apoptosis at days 1 and 5. Scale bars, 50 μm. AU, arbitrary units; ns, not significant. Photo Credit: Laetitia Andrique (INSERM U1029), Gaelle Recher (CNRS UMR 5298).

blood vessels in vivo had to be assessed. Since the default status of blood vessels under non-angiogenic, anti-inflammatory, and antithrombotic conditions is quiescence (*20*), we sought to evaluate the expression of the proliferative marker KI67 independently of the cell type (Fig. 2E). One day after tube formation, both vSMCs and HUVECs were highly proliferative [80%, as assessed by 4′,6-diamidino-2-phenylindole (DAPI) counterstaining]. At day 5, KI67 nuclear staining became undetectable, indicating that all cells were nonproliferative. As a control, we verified that this marked decrease in the fraction of proliferative cells was not concomitant with an increase in the number of apoptotic cells, which would indicate a collapsing vascular structure. Activated caspase-3 staining confirmed that cells were not undergoing apoptosis from day 1 to 5 (Fig. 2F) since only background level consistent with nonspecific noise was detected (*21*). Both proliferation and apoptosis marker detection indicated that HUVECs and vSMCs were in a quiescent state. The time required to reach homeostasis was mainly limited to the time necessary to obtain a complete and uniform coverage of the tube wall, and proliferation may help to fill up empty space in the cellular tube to reach a confluent cellular lining. An alternative way to reach more rapidly uniform coverage is to increase the total cell number in the tube and, thus, the total cell volume fraction in the CCS. For this purpose, we loaded the tubes with a cell concentration of 38% (in the same proportion as before; EC/SMC = 2:1) and found that not only the vesseloids were formed within 1 day but also HUVECs and vSMCs were quiescent at day 1, as evidenced by the absence of proliferation and apoptosis (fig. S6). This cell density is the practical limit above which tubes from the nozzle were irregular and became ill shaped. Together, our findings show that binary mixtures of ECs and SMCs were very efficiently guided toward a quiescent state in ECM-coated hollow tubes and that this process is sped up as the initial cell population is increased, leading to rapid contact inhibition and quiescence while not altering self-assembly (*22*). Vesseloids were then stable under these culture conditions for 1 to 2 weeks. After about 10 days, we observed cell delamination from the alginate shell and progressive collapse of the structure. Note that such an in vitro vesseloid stability is equivalent to the one reported in previous achievements of engineered vessels (*23*). Nonetheless, to demonstrate that stability could be further improved, we explored various culture conditions. In particular, vesseloids exhibited a prolonged stability under hypoxia (37°C, 5% CO_2, 0.1% O_2) compared to normoxia (fig. S7). This appreciable improvement needs to be explored in detail in future works and could be of primary importance for in vivo setting after grafting.

Tight junctions between ECs ensure vesseloid perfusability

To test whether vesseloids exhibit functional characteristics of blood vessels, we explored their perfusion and permeability properties. We developed a homemade perfusion device (Fig. 3, A and B) in which manually pulled glass pipettes inserted into the tubes and connected to a syringe pump were placed under a stereomicroscope. We injected solutions of fluorescent [fluorescein isothiocyanate (FITC)–coupled] dextran polymer of different molecular weights at a constant flow of 1 ml min^{-1} (Fig. 3, C and D, and movie S2). We imaged the fluorescent tubes (with or without cells) at the onset of dextran injection ($t = 0$) and after maintained perfusion for 10 min. We measured the cross-sectional intensity profile (Fig. 3E) to evaluate the penetration depth of the FITC-dextran probe within the alginate wall or within the composite material made of the alginate wall and cell layers. Since the alginate hollow fiber serves as a scaffold for vesseloid formation, we first needed to find a probe that diffuses freely through the alginate gels in the absence of cells to further evaluate whether the bound two-layered cellular structure reduced the permeability. We selected 500- and 20-kDa dextrans, characterized by hydrodynamic radii r_H of 3 and 15 nm, respectively (*24*). Although the fluorescence intensity profile measured with the 500-kDa dextran hardly broadened within 10 min (Fig. 3, C to E, row 1), the 20-kDa dextran rapidly invaded the alginate wall (Fig. 3, C to E, row 2). This behavior is consistent with previous reports of a mesh size for alginate gels in the range of 5 to 20 nm (*25*) and with theoretical obstruction models for molecular diffusion in heterogeneous gels such as alginate (*26*). From the measurement for the 20-kDa dextran, we estimated a minimal value for its effective diffusion coefficient, $D \sim L^2/t = 60\ \mu m^2\ s^{-1}$ (where L is the characteristic diffusion length; here, the thickness of the alginate wall), while the calculated value from Stokes-Einstein relation is $D = k_B T/(6\pi\eta r_H) = 70\ \mu m^2\ s^{-1}$, with η as the viscosity of water (10^{-3} Pa s) and $k_B T$ as the thermal energy. These calculations predict that the diffusion of dextran through the alginate is equivalent to free diffusion in water and depicts accurately what we observe. We then performed similar experiments with 20-kDa dextran injected into vesseloids that exhibit the above-described quiescent vessel-like structure, loaded with HUVECs only (Fig. 3, C to E, row 3) or with HUVECs and vSMCs (Fig. 3, C to E, row 4). As shown in Fig. 3D (row 4) and quantified in Fig. 3E, the probe penetration was hardly detectable (about 20% of the vessel + alginate thickness), indicating that HUVEC + vSMC layers significantly decrease the permeability cutoff of the tube. This is in agreement with recent intravital two-photon excitation fluorescence microscopy experiments showing that skin blood vessels restrict the passage of dextran larger than 20 kDa for at least the first 10 min following injection (*27*). Last, we evaluated vascular tubes only composed of HUVECs (Fig. 3, C to E, row 3) to determine whether vSMCs also contribute to the reduced permeability. Again, we observed 20-kDa dextran to hardly leak through the EC-based vesseloid (about 10% of the vessel + alginate thickness), suggesting that EC organization was sufficient to create a barrier that mimics the permeability properties of blood vessels. Since tight junctions are known to be instrumental in controlling the vascular permeability, we performed transmission electron microscopy (TEM) on vesseloids (Fig. 3, F to I). The presence of EC characteristics such as mature Weibel-Palade bodies (Fig. 3F) and the expression of abundant lamellar bodies (Fig. 3, G and H) suggests a functional self-organization of an endothelium (*28*). TEM micrographs also show an EC monolayer (Fig. 3I) (*29*) with tight junction between the cells (Fig. 3, G to I). A whole cross section of a vesseloid seen using TEM (fig. S8) also shows that SMC coverage of the endothelium is not complete. However, as described above, this does not jeopardize vesseloid perfusability, and as it will be seen below, these conditions are sufficient to allow vesseloid contractility in a range that is compatible with native blood vessel contractility. These findings indicate that the vesseloid wall recapitulates a major feature of a functional blood vessel wall and that a leak-free barrier is mainly provided by the sole endothelium.

Vesseloids exhibit vasoactivity

In blood vessels, one of the main functions of SMCs is contractility. To assess the vasoactivity of vesseloids, we primarily used endothelin-1 (ET-1). ET-1 is a peptide originally isolated from the vascular endothelium

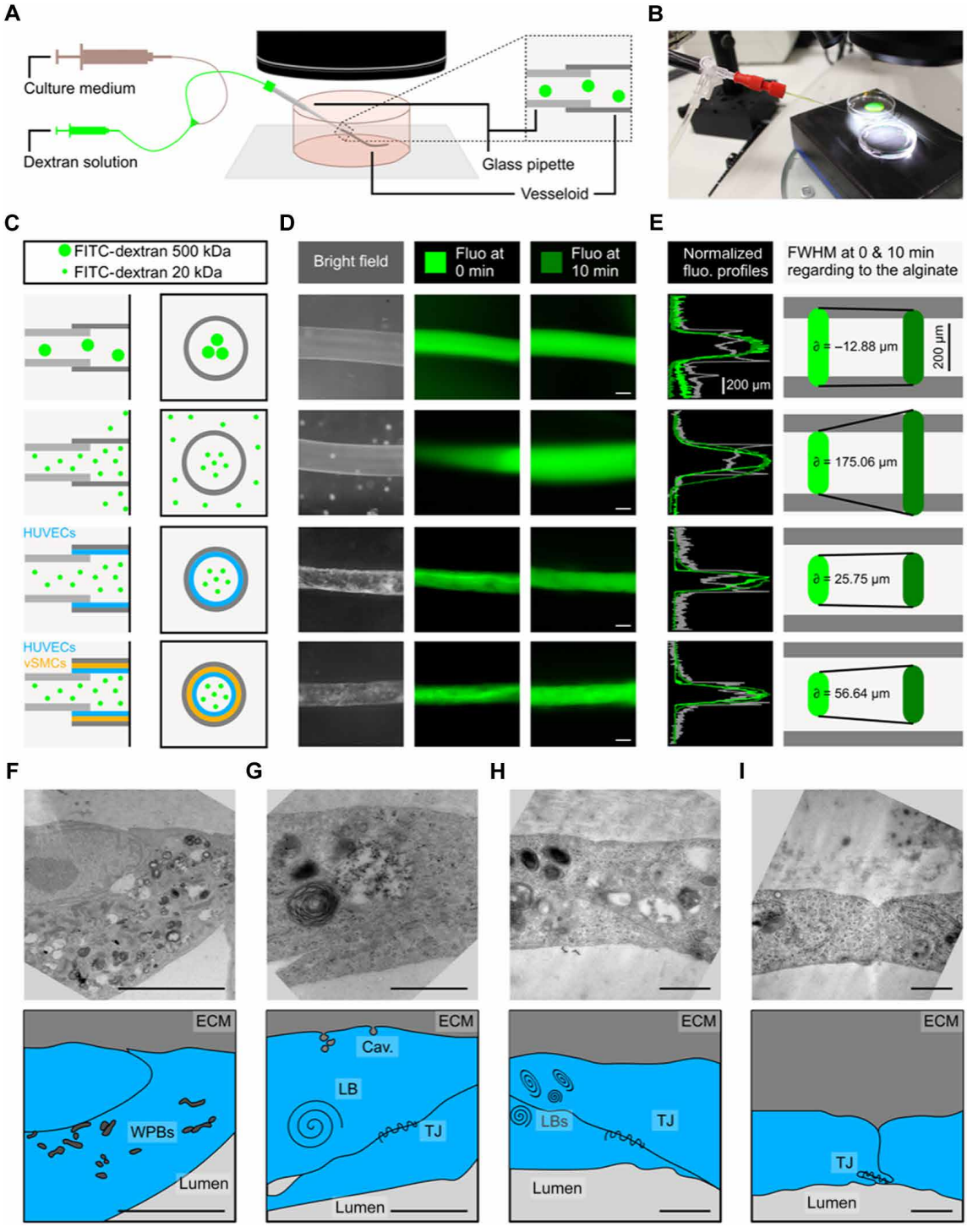

Fig. 3. Perfusable and liquid tight vesseloids. (**A**) Schematic drawing of the experimental design. The vesseloid is connected to a glass pipette for the perfusion of either dextran solution or culture medium for washing. (**B**) Photography of the perfusion device. (**C**) Schematic drawing of the experimental conditions. The left column depicts a longitudinal section alongside the glass pipet and the alginate tubes/vesseloids. The right column depicts the corresponding transverse sections. (**D**) Bright-field images of the tubes/vesseloids before perfusion (left column). Fluorescent images at *t*0 and 10 min after FITC-dextran perfusion (second and third columns). (**C** to **E**) Row 1: Alginate tube, perfusion of 500-kDa FITC-dextran. Row 2: Alginate tube, perfusion of 20-kDa FITC-dextran. Row 3: Vesseloid with HUVECs only, perfusion of 20-kDa FITC-dextran. Row 4: Vesseloid with HUVECs and vSMCs, perfusion of 20-kDa FITC-dextran. Scale bars, 200 µm. (**E**) Normalized fluorescence profiles both at the onset of FITC-dextran injection to mark the lumen size (0 min) and after 10 min, superimposed with the bright-field section. Corresponding fluorescence full width at half maximum (FWHM). (**F** to **I**) Vesseloids imaged by TEM at high magnification (×25,000 and ×50,000) after 1 day of culture. Corresponding drawing with identification of Weibel-Palade bodies (WPBs), lamellar bodies (LBs), tight junction (TJ), and caveolaes (Cav.). Scale bars, 5 µm. Photo Credit: Laetitia Andrique (INSERM U1029), Gaelle Recher (CNRS UMR 5298).

and further identified as a potent vasoconstrictor (*30*), although the mechanism has been long controversial due to the presence of multiple specific ET-1 receptors. ET_A receptors are only expressed in SMCs and mediate contractions, whereas ET_B receptors are present in both ECs and SMCs and induce a combination of SMC contraction and EC relaxation (*31*). We applied 0.1 μM ET-1 extraluminally (i.e., not by perfusion) and investigated the response of vesseloids in Fig. 4. From the fluorescent signal produced by Fluo-4 AM (see below), we measured the diameter of the vesseloid before and 6 min after ET-1 application (Fig. 4A). For approximately 50% of tested vesseloids, we detected a contraction by 5 ± 2.2% in diameter [Fig. 4A (top) and movie S3; $n = 12$], in agreement with previously reported contraction of rat coronary arteries perfused with ET-1 (*32*). This contractility response was confirmed by using another widely used vasoconstrictor agent, angiotensin (10 μM). In this case, we found a contraction of 5.6 ± 1.3% (Fig. 4A, bottom).

To further dissect the response to vasoconstrictor agents of SMCs and ECs separately, we monitored the ET-1–induced calcium response in Fig. 4 (B and C). To this aim, we first incubated vesseloids with 5 μM Fluo-4 AM as a Ca^{2+}-sensitive fluorescent probe (see Materials and Methods). Then, an individual vesseloid was immobilized with separate drops of agarose on both ends in a homemade microfabricated chamber (*33*). ET-1 was puffed locally nearby the agarose-free section, and the corresponding calcium-dependent fluorescence response was monitored over time in this section. Since the calcium probe is not cell specific, we developed an automated statistical cell sorting procedure based on principal components analysis (PCA) of systematically extracted measurements of single-cell fluorescent intensity kinetics. The whole procedure is depicted in Fig. 4B. In a trial and error method in which parameters such as maximal fluorescence intensity, "time-to-peak" respective to ET-1 application, circularity, and cell surface were selected by pairs as potentially correlated parameters, we found that the most discriminating parameters allowing to sort out cells into two subpopulations were the time to peak (from ET-1 application to half-time value of the rising edge of the first fluorescence intensity peak) and the cell surface. From this analysis, we observed that both HUVECs and vSMCs exhibited at first a primary response identified as the first and biggest intensity peak, followed by several Ca^{2+} oscillations [Fig. 4B (individual plots) and movie S4], suggesting synchronized calcium signaling between HUVECs and vSMCs (*34*). Moreover, cells identified as HUVECs were found to be significantly bigger (in average) than vSMCs and respond faster to ET-1 application (dot plots and sorted traces in Fig. 4C). These functional analyses based on the unsupervised sorting of the two cell populations open new ways for differential functional analysis because a more accurate description of the calcium kinetics is provided for each cell type individually and in relation with each other.

DISCUSSION

Because of thrombogenicity issues inherent to the use of synthetic grafts, tissue-engineered blood vessels (TEBVs) have long been considered as a necessary development for vascular repair strategies and are still the subject of intensive research in tissue engineering despite the fact that the construction of the first in vitro blood vessel dates back to 1986 (*35*). This very first TEBV was obtained by casting a mix of SMCs and collagen in an annular mold. After reinforcement with a synthetic fabric and removal of the mold, the tube was filled with ECs that eventually formed an endothelium. Together, the process took more than 2 weeks. Since one critical step in the procedure is the extraction from the annular mold, refined strategies consisted of using only biodegradable polymeric scaffolds (*36*) or no synthetic compound at all. L'Heureux *et al.* (*37*) managed to produce TEBVs based exclusively on biological material by culturing sheets of SMCs that were rolled before seeding ECs. Combination of the rolling technique with the bioabsorbable fibrous scaffold has recently led to the remarkable formation of TEBVs from adipose-derived stem cells (*38*). All these approaches allow us to generate large vessels in the size range of arteries (4 to 10 mm) and require a complex and long sequence of careful manipulations (2 to 8 weeks). With the advent of microfluidics, microfabrication, and 3D printing applied to biological matter, these approaches could be automated and extended to the formation of preformed or de novo vascular networks or to small-diameter vessels (*15*, *39*). The counterpart of this procedure simplification is that most aforementioned achievements were limited to the formation of endothelial tubes lacking an SMC sheath. To the best of our knowledge, there are two notable exceptions. Kawakami and colleagues (*40*) reported a five-step fabrication of tubular constructs from ECs embedded in a gelatin-alginate matrix fiber and SMCs that were seeded onto the outer wall before dissolution of the matrix. Munn and co-workers (*41*) managed to produce vascularized tumor explants in which the vasculature was self-assembled from cocultures of ECs and SMCs without an ECM. Although the vasculature consisting of multilayered tissues of SMCs underneath and above the endothelial network has the proper histoarchitecture, it takes about 14 days to establish, and the SMC-to-EC ratio and the seeding sequence are two critical parameters that strongly affect network formation.

By contrast, in the present work, we propose a strategy and report a proof of concept for a simple (in one step), rapid (in 1 day) and robust preparation of engineered functional blood vessels composed of an EC lining and an SMC sheath. To do so, we used the alginate hollow fiber technology to control the size of the vesseloids and took advantage of the conceptual possibility to orient cell self-assembly, as demonstrated by Gartner and co-workers (*14*), who showed that luminal and basal epithelial cells from the mammary gland self-organize in the incorrect configuration when cultured in agarose. However, this led to a polarization of a microtissue and lumen formation within 3 days upon embedding in Matrigel. While addition of soluble factors may a priori promote morphogenic processes, soluble factors released by Matrigel were discarded as regulators of self-organization. The ability of Matrigel (in contrast to agarose) to interact with cells and decrease the interfacial energy between cells and boundary was proposed as the driving mechanism (*14*). Our approach offers an additional validation of the universality of this concept that allows guiding cell self-assembly by tuning cell-matrix interactions. Mixed HUVECs and vSMCs seeded on a nonadhesive surface have been shown to sort out and form spheroidal cocultures with an outer layer composed of ECs and an SMC-rich core (*11*, *22*). On the basis of the findings reported in this work, we claim that the introduction of a micrometer-thick layer of Matrigel anchored to an initially nonadhesive alginate layer is sufficient to revert the configuration toward the correct architecture. One may, however, argue that the present configuration, which is tubular instead of spherical, could also alter the self-organization process. To critically test that the geometry of the scaffold is not determinant, we performed additional experiments in which ECs

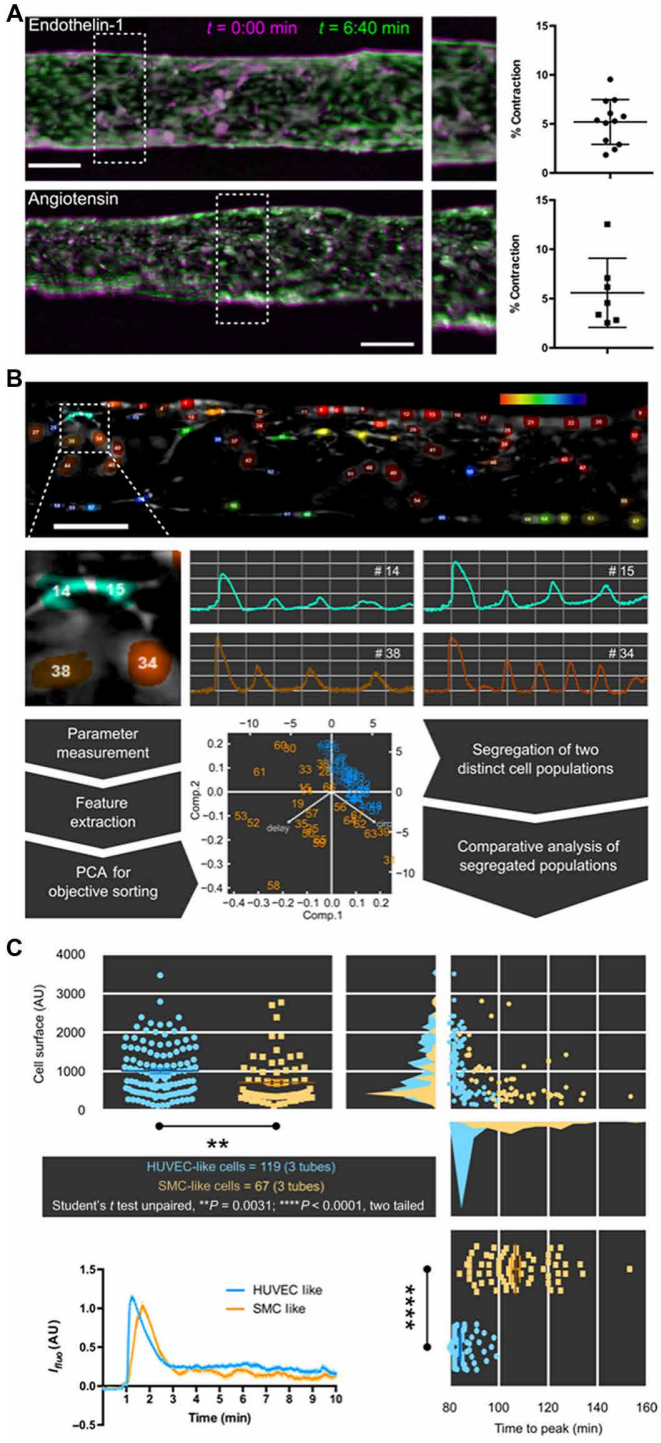

Fig. 4. Functional properties of vesseloids: Contractility and excitability. (**A**) Contraction assay. Vesseloids were exposed to 0.1 μM ET-1 (top) and to 10 μM angiotensin II, and subsequent contraction was measured. Left: Overlay of the first image before vasoconstrictor application (magenta) overlaid with the image at maximal contraction (green). Right: Percentage of contraction measured from the difference of the tube diameter before and after drug application. (**B**) Calcium imaging analysis subsequent to ET-1 application: Methodology. Top: Color-coded representation of a vesseloid. Cells that exhibit the earliest increase of fluorescence are depicted in red, whereas cells that responded the latest are colored in blue. Scale bars, 200 μm. Four cells are shown as examples (#14, #15, #38, and #34), and their respective fluorescence intensity variation is shown. From these individual traces, parameters were automatically extracted and sorted, notably by PCA with the following parameters: "delay" (time measured between ET-1 application and first fluorescence intensity peak) and "circ" (circularity of the cells, which depicts the cell shape), that allow the segregation of the two cell populations (HUVEC-like and SMC-like) used for further comparisons. (**C**) Calcium imaging analysis subsequent to ET-1 application: Results. Following segregation of the cell populations according to the previous description, traces were analyzed by comparing relevant parameters such as "cell surface" and time to peak, showing that the cell population identified as HUVECs exhibits a significantly bigger size and a faster response to ET-1 application than vSMCs. AU, arbitrary units.

and SMCs were encapsulated into spherical capsules internally coated with Matrigel following a previously published protocol (*16*). We also observed lumenization with EC lining and formation of an external SMC layer (fig. S9). The major difference with the tubular vesseloids was that the spherical vesseloid collapsed at day 2. We believe that this reduced stability is related to the restricted removal of cellular debris and the fact that convection is screened in these closed (spherical) microcompartments.

It is to emphasize that vesseloids retain many characteristics of functional blood vessels. ECs, in vesseloids, are connected via tight junction between each other to form a monolayer. They express VE-cadherin, VCAM-1, ICAM-1, integrins, and neuropillins and respond to inflammatory stimuli and vasoconstrictors. The expression of many of the aforementioned markers is enhanced in the vesseloids when compared to 2D monolayer cultures. This indicates that vesseloids provide a suitable 3D environment. The stability of vesseloids is comparable to previous engineered vessels of the order of 1 to 2 weeks. However, we found that hypoxia contributes to considerably increase the stability in vitro. We hypothesize that hypoxia may induce autocrine growth factor loops involving molecules such as vascular endothelial growth factors or fibroblast growth factors. Autocrine EC growth factor loops have been reported in earlier studies (*42*–*44*). The sole limitation of the present work is the lack of flexibility for controlling the coverage in SMCs and, in particular, the ability to produce multilayered SMC walls. We anticipate that this limitation, which does not hamper the production of functional vesseloids, will be overcome for larger vessels by adaptation of our fabrication protocol and upon in vivo graft leading to SMC recruitment from the host.

How can this directed cell self-assembly into functional vessels be explained at a molecular level? On the one hand, the ECM coating, which plays a determining role, constitutes the foundation for SMC anchoring. On the other hand, it is now well established that cells sense chemical and physical cues from the ECM, which, in turn, may affect cell functions, such as gene expression, contractility, or migration (*45*). Matrix-dependent effects include cell traction forces that increase with enhanced matrix stiffness. Of direct relevance here, a mechanical feedback between cells and the ECM through cell traction forces may lead to large-scale cellular organization (*46*).

Despite this bundle of reported hints on how cell-ECM interactions govern tissue architecture, it remains unclear at present how fast cell self-organization, as observed in our case, occurs with a rapid polarization of ECs and SMCs. At this stage, one may only speculate about the reasons for this different behavior. ECM-integrin interactions could be more affine for SMCs than for ECs, providing a rationale to explain why SMCs outcompete ECs for ECM binding and thus leads to SMC/EC polarization. Moreover, laminin, which is abundantly present in Matrigel, has been shown to play a pivotal role in SMC differentiation: Adhesion receptors to laminin, α1β1 and α7β1 integrins and α-dystroglycan, are indeed only expressed in contractile SMCs (*47*). Conversely, the interaction of ECs with Matrigel may generate an unfavorable environment for EC spreading and monolayer formation that could favor, by default, SMC spreading. It is known that ECs when cultured on the top of Matrigel undergo rapid morphological changes that convert EC monolayers to a cord-like network. This implies that de-adhesion must occur during the conversion process and, thus, that de-adhesion signals are conveyed by the Matrigel matrix. The balance between adhesion and de-adhesion to the matrix is different and favors adhesion of SMCs to the Matrigel layer.

Besides this cell self-assembly, we also showed that ECs form a leak-free barrier that is not disturbed by the SMC layer. Tight junctions were evidenced and contribute to maintain the cohesivity of the EC layer. Furthermore, vessel contractility is preserved in vesseloids, presumably mostly assigned to SMCs and triggered by the mechanical properties of SMCs (*48*). SMCs have plasticity and may exhibit a synthetic, migratory, or contractile phenotype, and it has been shown that contractile SMCs initially rounded up before spreading and migrating. These migratory cells are highly dynamic and establish communication with neighboring cells. Matrigel was reported to favor a contractile phenotype of SMCs with a decrease in mitogen-activated protein (MAP) kinase signaling (*49*). In mature blood vessels, SMCs are organized in tissues that have phenotypic plasticity, which allow them to oscillate from a proliferative, migratory, and synthetic state to a quiescent/contractile state depending on the environmental constraints and pathological conditions (*50*). A strict but not well-known control of SMC plasticity is required to prevent pathologies such as intimal hyperplasia or circulatory disorder such as pulmonary artery hypertension (*51*). In our experimental setting, a promigratory phenotype may be initially favored because cells are injected in the presence of serum and growth factors with cells circulating on the inner surface of the alginate tube. At a later stage, once a firm interaction with the matrix has been established, SMCs are fully converted into a contractile phenotype.

In summary, we have developed an efficient and rapid approach for producing artificial mature blood vessels. Vesseloids may serve as a suitable model to elucidate morphogenic processes of vascular development and signaling mechanisms for tissue/cell polarization.

However, this achievement could also be exploited for pharmacological testing, tissue regeneration purposes, and vascular grafting. The prevalent strategy for the replacement of large vessels (>4 to 6 mm) is the use of autologous or synthetic grafts. Specific issues to microvessels such as lumen collapse, easiness of handling, and maintenance of mechanical properties are solved with the vesseloids we developed. For further use of vesseloids in an autologous human context, the strategy of choice is the use of differentiated induced pluripotent stem cells that underwent reprogramming. Such a development will definitely make vesseloids a system of choice for regenerative medicine and vascular grafting.

MATERIALS AND METHODS

Cell culture and maintenance

HUVECs and SMCs (C-12205 and C-12511, PromoCell) were maintained in endothelial growth medium 2 (EGM2; C-22111, PromoCell) and SMC growth medium (SMCGM2; C-22062, PromoCell), respectively, under water-saturated 5% CO_2 atmosphere at 37°C. Cells were grown in collagen-I–coated flasks (10190103, Thermo Fisher Scientific) and detached at passage 5 for vesseloid formation.

Lentiviral production and cell transduction

HUVECs were infected by pLV-EBFP2-nuc (a gift from P. Tsoulfas; Addgene plasmid no. 36085), while SMCs were infected by hPGK-NLS-Tomato virus.

Microfluidic coextrusion device and 3D tube formation

The design of a coextrusion microfluidic device dedicated for spherical capsules formation has been previously described (*52*). Here, we slightly modified the design. The stereolithographic file

(STL) file used for 3D printing is provided as data file S1. Using this device, we produced alginate hollow tubes filled with both ECs and SMCs. Briefly, cells were injected into the central zone isolated from the 2.5% (w/v) AL by a 300 mM IS. Cell loading of the CCS varied from 33% (v/v) (routine conditions) to 38% (v/v) (maximum loading). Cells were dispersed in Matrigel (phenol red free: 354262, Corning). The cell mixture was composed of 2:1 HUVEC/vSMC (for example, 14 million ECs/7 million SMCs). Practically, for each encapsulation, we started from 300 cm^2 of HUVECs and 150 cm^2 of vSMCs. Fifty-five microliters of cell pellet was resuspended directly with 110 or 90 μl of Matrigel (for the 33 and 38% cell loadings, respectively). These conditions ensure that the final Matrigel concentration in the tubes is about 35% (v/v), which is sufficient to create a continuous Matrigel layer anchored to the inner alginate wall (*16*). Most experiments were performed using the following injection flow rates: 2 ml $hour^{-1}$ (AL), 1 ml $hour^{-1}$ (IS), and 1 ml $hour^{-1}$ (CCS). The impact of flow rates variation on the homogeneity of the tubes was investigated in Fig. 1C. A 100 mM calcium bath at 37°C was used to trigger rapid gelation of the alginate gel while avoiding osmotic shock. Immediately after formation (within less than 10 min), the tubes were transferred in HUVEC and vSMC growth medium mixture (1:1 EGM2/SMCGM2) and incubated at 37°C. This procedure developed for vesseloid preparation was patented (please see details in Acknowledgments).

Immunofluorescence analysis

Vesseloids were fixed in 4% paraformaldehyde (F8775, Sigma-Aldrich) overnight at 4°C before a 30-min permeabilization at room temperature in Dulbecco's modified Eagle's medium (DMEM; P04-05545, PAN Technology) and 0.1% Triton X-100. Nonspecific sites were saturated by 1% bovine serum albumin and 2% fetal bovine serum in DMEM for 1 hour at 4°C under agitation. Vesseloids were then incubated at 4°C overnight under shaking, with an anti-CD31 sheep polyclonal antibody (1:100; AF806, R&D), anti-αSMA mouse monoclonal antibody (1:100; MAB1420, R&D), anti-tubulin mouse monoclonal antibody (1:100; T5168, Sigma), anti-laminin rabbit polyclonal antibody (1:100; AB30320, Abcam), anti–VE-cadherin (1:100; SC6458, Santa Cruz Biotechnology), or anti–fibrillin-1 (1:100; AB53075, Abcam). After three 15-min washes with DMEM, vesseloids were reacted with the corresponding secondary antibody (anti-mouse, anti-sheep, anti-rabbit) coupled with Alexa Fluor 488, 546 or 647 (1:400; Molecular Probes) for 1 hour at 4°C. After rinsing three more times with DMEM, vesseloids were incubated for 20 min with DAPI (1 μg ml^{-1}; D9542, Sigma-Aldrich) before imaging.

Optical microscopy and image analysis

One-centimeter-long fixed and immunostained vesseloid portions were included in 1% low gelling agarose (A9414, Sigma-Aldrich) within the tailored wells of the UniverSlide (*33*) filled with DMEM. Confocal images of vascular tubes were acquired with a Nikon Eclipse Ti inverted microscope equipped with a C2Si scan head acquisition software (NIS-Element, NIS). Image analysis was performed with Fiji (https://fiji.sc/).

Proliferation and apoptosis measurement

Vesseloids were immunostained by an anti-CD31 sheep polyclonal antibody (1:200; AF806, R&D) and either an anti-activated caspase-3 rabbit polyclonal antibody (1:200; G748, Promega) or anti-KI67 monoclonal antibody (1:200; M7240, Dako) before DAPI staining, as described above. We chose two time points, days 1 and 5, after tube formation. Nuclear KI67 and activated caspase-3 signals were quantified using Fiji (https://fiji.sc/), on the same tube length (400 μm), and compared at days 1 and 5.

Perfusion experiments

One day after formation, 3 cm of cell-free and cell-laden tubes (HUVECs + vSMCs) were cannulated using a homemade perfusion device made of glass capillary connected to a peristaltic pump. The 500-kDa FITC-dextran (FD500S, Sigma-Aldrich) and 20-kDa FITC-dextran (FD20, Sigma-Aldrich), at 100 mg ml^{-1} each, were injected into the lumen at one opened side of the tube, at a continuous flow rate of 1 ml min^{-1}. FITC-dextran was then released in the medium from the opposite tube end, generating a fluorescent plume. Release of the fluorescent probe into the medium contributed to a fluorescent background increasing in time. To circumvent this difficulty, the permeability of the tubes was assessed by analyzing the diffusion of the FITC-dextran through the alginate walls. Visualization was performed using a fluorescent microscope (Nikon SMZ 18) for 10 min.

Transmission electron microscopy

Twenty-four hours after tube formation, vesseloids were fixed in 2% paraformaldehyde and 2% glutaraldehyde (20879.238, VWR) overnight at 4°C. After three washes for 5 min in 0.1 M PB (phosphate buffer), vesseloids were stained with 1% OsO_4 in 0.1 M PB before dehydration and impregnation in epoxy resin. Cross sections of the vesseloids were imaged with a Hitachi H7650 electron microscope at high magnification (×25,000 and ×50,000) at the Bordeaux Imaging Center microscopy facility.

Calcium imaging and contractility measurement

Intracellular Ca^{2+} variations were monitored on day 1 of vesseloids loaded with 5 μM (final concentration) Fluo-4 AM calcium probe (F23917, Thermo Fisher Scientific). Briefly, the dye solution was prepared as follows: 10 μg of powder was dissolved in 4 μl of Pluronic F-127 (P3000MP, Thermo Fisher Scientific), sonicated for 10 min, and diluted to the final concentration in standard medium. Vesseloids were incubated for 45 min at 37°C, then transferred to fresh medium, and imaged with a stereomicroscope (Nikon SMZ 18). We locally applied 0.1 μM ET-1 (E7764, Sigma-Aldrich) or 10 μM angiotensin II (A9525, Sigma Aldrich), and fluorescence was collected with a 10× objective and directed through a 525/50 band-pass filter to the camera. The acquired images were first processed for registration with available ImageJ plugin (StackReg). We then analyzed the registered images with a homemade LabView-based (National Instruments) software. The algorithm workflow was the following: (i) The background was subtracted using a region outside of the tube in each image. (ii) The temporal variation of fluorescence was then extracted pixel by pixel. (iii) Pixel fluorescence variations along the entire acquisition were used for automated segmentation of the cells (watershed based segmentation). (iv) For each segmented cell, time to peak and morphological features were computed.

The effect of ET-1 and angiotensin on in vivo contractility is classically shown by measuring the change in vascular tone (*32*). Since one advantage of the vesseloid model is that it is manipulable, contraction could be assessed here by handling vesseloids inside an imaging chamber and by directly measuring the diameter of the vesseloid before drug application and at maximal contraction. Image contrast was enhanced and normalized for the whole movie to improve the contrast at the border of the vesseloid and to compensate for

photobleaching. A line with a width of 10 pixels was drawn perpendicularly to the main vesseloid axis and was used to measure the distance between the two walls. The percentage of contraction was defined as the relative diameter variation between resting and contracted states of the vesseloid.

RT-qPCR analysis

ECs were obtained from either direct HUVECs (2D culture on Matrigel coating versus 3D in vesseloids) or $CD31^+$ cells after CD31 magnetic bead sorting (HUVECs + SMCs on Matrigel-coated 2D culture versus HUVECs + SMCs in vesseloids). RNAs were extracted (RNeasy mini plus kit, 74134, QIAGEN) and reverse-transcribed (high-capacity cDNA reverse transcription kit, 4368814, Applied Biosystems). qPCR analysis was performed with the same amount of resulting cDNA using the following primers: PODXL, AACCCGGCCCAAGATAAGTG (forward) and GGCAGGGAGCTTAGTGTGAA (reverse); ITGβ1, GAAGGGTTGCCCTCCAGA (forward) and GCTTGAGCTTCTCTGCTGTT (reverse); NRP1, CAAGGCGAAGTCTTTTGAGG (forward) and CACCTGTGAGCTGGAAGTCA (reverse); NRP2 CTGTGGGTCATCCGTGAGGAC (forward) and ATGGGTTCCATGCAGTTCTCCAG (reverse); VCAM-1, CGTCTTGGTCAGCCCTTCCT (forward) and ACATTCATATACTCCCGCATCCTTC (reverse); ICAM-1 AGGCCACCCCAGAGGACAAC (forward) and ICAM-1 CCCATTATGACTGCGGCTGCTA (reverse); and GAPDH, CTGCACCACCAACTGCTTAG (forward) and AGGTCCACCACTGACACGTT (reverse).

Statistical analysis

Statistical analysis was performed using GraphPad Prism 5 software (GraphPad, La Jolla, CA) using one-sample *t* test, Mann-Whitney *U* test, or paired *t* test for ET-1 contractility measurement. For all statistics, the *n* value used to calculate the statistics is given in the figure legends. $^{****}P < 0.0001$, $^{***}P < 0.001$, $^{**}P < 0.01$, $^{*}P < 0.05$, and bars represent means ± SD.

SUPPLEMENTARY MATERIALS

Supplementary material for this article is available at http://advances.sciencemag.org/cgi/content/full/5/6/eaau6562/DC1

Fig. S1. Dimension and shape of the coextrusion chip.
Fig. S2. Uniform laminin coating of the inner alginate wall.
Fig. S3. Diameter tube measurement using three coextrusion devices of different nozzle sizes.
Fig. S4. Immunostainings of CD31, fibrillin-1, and VE-cadherin were performed on vesseloids at day 1.
Fig. S5. Expression measurement of (i) basal and luminal markers, (ii) arterial and venous markers, and (iii) endothelial activation markers in regular culture conditions and in response to inflammatory stimuli.
Fig. S6. Quiescent cells at day 1 by loading the maximum of cells in the vesseloids.
Fig. S7. Hypoxia culture stabilizes the vesseloids.
Fig. S8. Vesseloid imaged by TEM at high magnification (×25,000 and ×50,000) after 1 day of culture.
Fig. S9. Lumenization with EC lining and formation of an external SMC layer in spherical capsules.
Movie S1. ECs and SMCs are dynamic after encapsulation.
Movie S2. The 20-kDa FITC-dextran perfusion.
Movie S3. ET-1 induces vesseloid contraction.
Movie S4. ET-1 induces intracellular calcium raise in both ECs and SMCs.
Data file S1. STL file of the coextrusion chip.

REFERENCES AND NOTES

1. E. Cukierman, R. Pankov, D. R. Stevens, K. M. Yamada, Taking cell-matrix adhesions to the third dimension. *Science* **294**, 1708–1712 (2001).
2. E. K. Hendow, P. Guhmann, B. Wright, P. Sofokleous, N. Parmar, R. M. Day, Biomaterials for hollow organ tissue engineering. *Fibrogenesis Tissue Repair* **9**, 3 (2016).
3. Y. K. Kurokawa, S. C. George, Tissue engineering the cardiac microenvironment: Multicellular microphysiological systems for drug screening. *Adv. Drug Deliv. Rev.* **96**, 225–233 (2016).
4. F. Zheng, F. Fu, Y. Cheng, C. Wang, Y. Zhao, Z. Gu, Organ-on-a-Chip Systems: Microengineering to biomimic living systems. *Small* **12**, 2253–2282 (2016).
5. S. N. Bhatia, D. E. Ingber, Microfluidic organs-on-chips. *Nat. Biotechnol.* **32**, 760–772 (2014).
6. J. Jang, H.-G. Yi, D.-W. Cho, 3D printed tissue models: Present and future. *ACS Biomater Sci. Eng.* **2**, 1722–1731 (2016).
7. S. V. Murphy, A. Atala, 3D bioprinting of tissues and organs. *Nat. Biotechnol.* **32**, 773–785 (2014).
8. H.-W. Kang, S. J. Lee, I. K. Ko, C. Kengla, J. J. Yoo, A. Atala, A 3D bioprinting system to produce human-scale tissue constructs with structural integrity. *Nat. Biotechnol.* **34**, 312–319 (2016).
9. D. B. Kolesky, K. A. Homan, M. A. Skylar-Scott, J. A. Lewis, Three-dimensional bioprinting of thick vascularized tissues. *Proc. Natl. Acad. Sci.* **113**, 3179–3184 (2016).
10. F. Marga, A. Neagu, I. Kosztin, G. Forgacs, Developmental biology and tissue engineering. *Birth Defects Res. C Embryo Today* **81**, 320–328 (2007).
11. K. Jakab, C. Norotte, F. Marga, K. Murphy, G. Vunjak-Novakovic, G. Forgacs, Tissue engineering by self-assembly and bio-printing of living cells. *Biofabrication* **2**, 022001 (2010).
12. M. Peck, N. Dusserre, T. N. McAllister, N. L'Heureux, Tissue engineering by self-assembly. *Mater. Today* **14**, 218–224 (2011).
13. R. A. Foty, M. S. Steinberg, The differential adhesion hypothesis: A direct evaluation. *Dev. Biol.* **278**, 255–263 (2005).
14. A. E. Cerchiari, J. C. Garbe, N. Y. Jee, M. E. Todhunter, K. E. Broaders, D. M. Peehl, T. A. Desai, M. A. LaBarge, M. Thomson, Z. J. Gartner, A strategy for tissue self-organization that is robust to cellular heterogeneity and plasticity. *Proc. Natl. Acad. Sci. U.S.A.* **112**, 2287–2292 (2015).
15. H. Onoe, T. Okitsu, A. Itou, M. Kato-Negishi, R. Gojo, D. Kiriya, K. Sato, S. Miura, S. Iwanaga, K. Kuribayashi-Shigetomi, Y. T. Matsunaga, Y. Shimoyama, S. Takeuchi, Metre-long cell-laden microfibres exhibit tissue morphologies and functions. *Nat. Mater.* **12**, 584–590 (2013).
16. K. Alessandri, M. Feyeux, B. Gurchenkov, C. Delgado, A. Trushko, K.-H. Krause, D. Vignjević, P. Nassoy, A. Roux, A 3D printed microfluidic device for production of functionalized hydrogel microcapsules for culture and differentiation of human Neuronal Stem Cells (hNSC). *Lab Chip* **16**, 1593–1604 (2016).
17. H.-S. Kim, A kinetic study on calcium alginate bead formation. *Korean J. Chem. Eng.* **7**, 1–6 (1990).
18. J. Thyberg, A. Hultgårdh-Nilsson, Fibronectin and the basement membrane components laminin and collagen type IV influence the phenotypic properties of subcultured rat aortic smooth muscle cells differently. *Cell Tissue Res.* **276**, 263–271 (1994).
19. E. M. Conway, New specs for arteriovenous identity. *Blood* **122**, 3857–3858 (2013).
20. E. A. Jaffe, Cell biology of endothelial cells. *Hum. Pathol.* **18**, 234–239 (1987).
21. S. Sorrells, C. Toruno, R. A. Stewart, C. Jette, Analysis of apoptosis in zebrafish embryos by whole-mount immunofluorescence to detect activated Caspase 3. *J. Vis. Exp.* **2013**, e51060 (2013).
22. T. Korff, S. Kimmina, G. Martiny-Baron, H. G. Augustin, Blood vessel maturation in a 3-dimensional spheroidal coculture model: Direct contact with smooth muscle cells regulates endothelial cell quiescence and abrogates VEGF responsiveness. *FASEB J.* **15**, 447–457 (2001).
23. V. Catto, S. Farè, G. Freddi, M. C. Tanzi, Vascular tissue engineering: Recent advances in small diameter blood vessel regeneration. *ISRN Vasc. Med.* **2014**, 923030 (2014).
24. J. K. Armstrong, R. B. Wenby, H. J. Meiselman, T. C. Fisher, The hydrodynamic radii of macromolecules and their effect on red blood cell aggregation. *Biophys. J.* **87**, 4259–4270 (2004).
25. H. Tanaka, M. Matsumura, I. A. Veliky, Diffusion characteristics of substrates in Ca-alginate gel beads. *Biotechnol. Bioeng.* **26**, 53–58 (1984).
26. B. Amsden, Solute diffusion within hydrogels. mechanisms and models. *Macromolecules* **31**, 8382–8395 (1998).
27. G. Egawa, S. Nakamizo, Y. Natsuaki, H. Doi, Y. Miyachi, K. Kabashima, Intravital analysis of vascular permeability in mice using two-photon microscopy. *Sci. Rep.* **3**, 1932 (2013).
28. J. W. Dobbie, J. D. Anderson, Ultrastructure, distribution, and density of lamellar bodies in human peritoneum. *Perit. Dial. Int.* **16**, 482–487 (1996).
29. N. Jiménez, V. J. D. Krouwer, J. A. Post, A new, rapid and reproducible method to obtain high quality endothelium in vitro. *Cytotechnology* **65**, 1–14 (2013).
30. M. Yanagisawa, H. Kurihara, S. Kimura, Y. Tomobe, M. Kobayashi, Y. Mitsui, Y. Yazaki, K. Goto, T. Masaki, A novel potent vasoconstrictor peptide produced by vascular endothelial cells. *Nature* **332**, 411–415 (1988).
31. S. Taddei, A. Virdis, L. Ghiadoni, I. Sudano, M. Notari, A. Salvetti, Vasoconstriction to endogenous endothelin-1 is increased in the peripheral circulation of patients with essential hypertension. *Circulation* **100**, 1680–1683 (1999).

32. A. D. Giulumian, M. M. Molero, V. B. Reddy, J. S. Pollock, D. M. Pollock, L. C. Fuchs, Role of ET-1 receptor binding and $[Ca^{2+}]_i$ in contraction of coronary arteries from DOCA-salt hypertensive rats. *Am. J. Physiol.Heart Circ. Physiol.* **282**, H1944–H1949 (2002).
33. K. Alessandri, L. Andrique, M. Feyeux, A. Bikfalvi, P. Nassoy, G. Recher, All-in-one 3D printed microscopy chamber for multidimensional imaging, the *UniverSlide*. *Sci. Rep.* **7**, 42378 (2017).
34. T. Burdyga, L. Borysova, Calcium signalling in pericytes. *J. Vasc. Res.* **51**, 190–199 (2014).
35. C. B. Weinberg, E. Bell, A blood vessel model constructed from collagen and cultured vascular cells. *Science* **231**, 397–400 (1986).
36. L. E. Niklason, J. Gao, W. M. Abbott, K. K. Hirschi, S. Houser, R. Marini, R. Langer, Functional arteries grown in vitro. *Science* **284**, 489–493 (1999).
37. N. L'Heureux, S. Pâquet, R. Labbé, L. Germain, F. A. Auger, A completely biological tissue-engineered human blood vessel. *FASEB J.* **12**, 47–56 (1998).
38. R. Zhou, L. Zhu, S. Fu, Y. Qian, D. Wang, C. Wang, Small diameter blood vessels bioengineered from human adipose-derived stem cells. *Sci. Rep.* **6**, 35422 (2016).
39. S. Raghavan, C. M. Nelson, J. D. Baranski, E. Lim, C. S. Chen, Geometrically controlled endothelial tubulogenesis in micropatterned gels. *Tissue Eng. Part A* **16**, 2255–2263 (2010).
40. S. Sakai, S. Yamaguchi, T. Takei, K. Kawakami, Oxidized alginate-cross-linked alginate/gelatin hydrogel fibers for fabricating tubular constructs with layered smooth muscle cells and endothelial cells in collagen gels. *Biomacromolecules* **9**, 2036–2041 (2008).
41. D. Bazou, N. Maimon, G. Gruionu, L. L. Munn, Self-assembly of vascularized tissue to support tumor explants in vitro. *Integr. Biol.* **8**, 1301–1311 (2016).
42. B. L. Krock, N. Skuli, M. C. Simon, Hypoxia-induced angiogenesis: Good and evil. *Genes Cancer* **2**, 1117–1133 (2011).
43. A. Zimna, M. Kurpisz, Hypoxia-inducible factor-1 in physiological and pathophysiological angiogenesis: Applications and therapies. *Biomed. Res. Int.* **2015**, 549412 (2015).
44. N. Campillo, B. Falcones, J. M. Montserrat, D. Gozal, A. Obeso, T. Gallego-Martin, D. Navajas, I. Almendros, R. Farré, Frequency and magnitude of intermittent hypoxia modulate endothelial wound healing in a cell culture model of sleep apnea. *J. Appl. Physiol.* **123**, 1047–1054 (2017).
45. D. E. Discher, P. Janmey, Y.-L. Wang, Tissue cells feel and respond to the stiffness of their substrate. *Science.* **310**, 1139–1143 (2005).
46. S. Checa, M. K. Rausch, A. Petersen, E. Kuhl, G. N. Duda, The emergence of extracellular matrix mechanics and cell traction forces as important regulators of cellular self-organization. *Biomech. Model. Mechanobiol.* **14**, 1–13 (2015).
47. E. P. Moiseeva, Adhesion receptors of vascular smooth muscle cells and their functions. *Cardiovasc. Res.* **52**, 372–386 (2001).
48. M. J. Berridge, Smooth muscle cell calcium activation mechanisms. *J. Physiol.* **586**, 5047–5061 (2008).
49. X. Li, P. Tsai, E. D. Wieder, A. Kribben, V. Van Putten, R. W. Schrier, R. A. Nemenoff, Vascular smooth muscle cells grown on Matrigel. A model of the contractile phenotype with decreased activation of mitogen-activated protein kinase. *J. Biol. Chem.* **269**, 19653–19658 (1994).
50. J. Pelisek, S. Armeanu, S. Nikol, Quiescence, cell viability, apoptosis and necrosis of smooth muscle cells using different growth inhibitors. *Cell Prolif.* **34**, 305–320 (2001).
51. S. F. Louis, P. Zahradka, Vascular smooth muscle cell motility: From migration to invasion. *Exp. Clin. Cardiol.* **15**, e75–e85 (2010).
52. K. Alessandri, B. R. Sarangi, V. V. Gurchenkov, B. Sinha, T. R. Kießling, L. Fetler, F. Rico, S. Scheuring, C. Lamaze, A. Simon, S. Geraldo, D. Vignjević, H. Doméjean, L. Rolland, A. Funfak, J. Bibette, N. Bremond, P. Nassoy, Cellular capsules as a tool for multicellular spheroid production and for investigating the mechanics of tumor progression in vitro. *Proc. Natl. Acad. Sci. U.S.A.* **110**, 14843–14848 (2013).

Acknowledgments: TEM was performed at the Bordeaux Imaging Center (a service unit of the CNRS-INSERM and Bordeaux University, member of the national infrastructure France BioImaging), and we are thankful to E. Gontier, M. Petrel, S. Lacomme, and P. Teulat for technical help. **Funding:** This work was supported by the ANR VascTubes (ANR-15-CE18-0019) and MecaTiss (ANR- 7-CE30-0007-03) to A.B. and P.N. L.A. was supported by the Fondation Lefoulon Delalande, Institut de France. G.R. is a member of the CNRS ImaBio GdR. **Author contributions:** L.A., G.R., P.N., and A.B. wrote the manuscript. G.R., K.A., and M.F. design and printed the 3D microfluidic device. L.A. and G.R. performed together all experiments regarding tube formation and 3D confocal and videomicroscopy analysis, perfusion, and contractility measurements. N.P. performed TEM experiments and analysis. L.A. performed lentivector cloning, infections, and immunostainings. G.R. performed video analysis. G.R., P.B., and L.C. designed and performed an automated procedure for calcium imaging. L.A., G.R., P.N., and A.B. contributed to experimental design and interpretation. **Competing interests:** L.A., G.R., K.A., M.F., P.N., and A.B. are inventors on a patent related to this work (no. WO2018162857; International Application no. PCT/FR2018/050541, published on 13 September 2018, filed on 8 March 2018). The authors declare that they have no other competing interests. **Data and materials availability:** All data needed to evaluate the conclusions in the paper are present in the paper and/or the Supplementary Materials. Additional data related to this paper may be requested from the authors.

Submitted 3 July 2018
Accepted 10 May 2019
Published 12 June 2019
10.1126/sciadv.aau6562

Citation: L. Andrique, G. Recher, K. Alessandri, N. Pujol, M. Feyeux, P. Bon, L. Cognet, P. Nassoy, A. Bikfalvi, A model of guided cell self-organization for rapid and spontaneous formation of functional vessels. *Sci. Adv.* **5**, eaau6562 (2019).